Research Article Vol. 57, No. 14 / 10 May 2018 / Applied Optics 3983

applied optics

Three-dimensional shape measurement using a structured light system with dual projectors

Chufan Jiang, Beatrice Lim, and Song Zhang*

School of Mechanical Engineering, Purdue University, West Lafayette, Indiana 47907, USA
*Corresponding author: szhang15@purdue.edu

Received 20 March 2018; revised 16 April 2018; accepted 16 April 2018; posted 17 April 2018 (Doc. ID 326460); published 10 May 2018

This paper introduces a structured light system with two projectors and one camera for three-dimensional (3D) shape measurement to alleviate problems created by a single projector such as the shadow problem. In particular, we developed (1) a system calibration framework that can accurately calibrate each such camera-projector system; (2) a residual error correction method based on the system error function; and (3) a data fusion method utilizing the angle between the projection direction and surface normal. Experimental results demonstrate that the proposed dual-projector structured light system improves the measurement accuracy besides extending the measurement range of a single projector system.

OCIS codes: (120.0120) Instrumentation, measurement, and metrology; (100.5070) Phase retrieval; (120.2650) Fringe analysis; (150.6910) Three-dimensional sensing.

https://doi.org/10.1364/AO.57.003983

1. INTRODUCTION

Optical three-dimensional (3D) shape measurement has vast applications in the fields of manufacturing industry, computer graphics, entertainment, and biomedical disease diagnosis [1]. The structured light method based on digital fringe projection (DFP) technology has generated great popularity in optical metrology because of its high-speed high-resolution capability and non-contact nature [2].

A structured light system typically consists of a single camera and a single projector. In such a system, the field of view is limited by the common area of two devices. Some novel techniques have been developed to deal with problems caused by the single camera. Zhang and Yau [3] proposed a structured light system with dual cameras to alleviate camera occlusion and addressed corresponding problems on dual-camera one-projector system calibration and data fusion. Zhang *et al.* [4] developed a multi-resolution system to simultaneously obtain the whole profile and particular high accuracy details. Liu *et al.* [5] used cameras from different angles to alleviate saturated regions caused by specular reflection in single camera images. Instead of improving measurement quality, another group of studies utilized multiple cameras to obtain additional information for absolute phase unwrapping [6–8].

On the other hand, single-projector-based structured light system has its unique limitations. One of the typical problems is the shadow created by a single projection angle, as illustrated in Fig. 1(a). In the red shaded area, structured patterns from the projector cannot be shined onto the object surface, yet the camera can capture a shadow region. To reduce shadow regions, one can rotate the object for different scans and register those data obtained from different orientations. However, such an approach is not desirable for high-speed applications or measuring dynamically deformable objects. If there is a second projector in the system, as shown in Fig. 1(b), each projector separately projects the structured patterns from a different angle, and the camera captures images for both projections. Since different projectors generate shadows on different regions, we can obtain the 3D measurement from each projector-camera pair and combine them into one complete result to alleviate shadow problems from a single projector.

For areas where both projectors can properly illuminate, a second projector also provides an additional measurement from another angle. Fringe patterns projected from two projectors distort differently on the object surface and provide different measurement quality. We quantify the measurement quality by calculating the projection angle between the projection direction and object surface normal. When the angle between the projector and the camera is not large, a smaller projection angle provides higher measurement accuracy because the spatial resolution of the projected fringe pattern is higher. Based on angle calculation, we can decide better 3D data from two projectors point by point and merge them into a single result with the best measurement quality.

In this research, we propose a calibration framework for the two-projector one-camera structured light system. Each device is calibrated independently for intrinsic parameter estimation. Then extrinsic parameters for the whole system are calibrated under the same world coordinate so that reconstructed surfaces

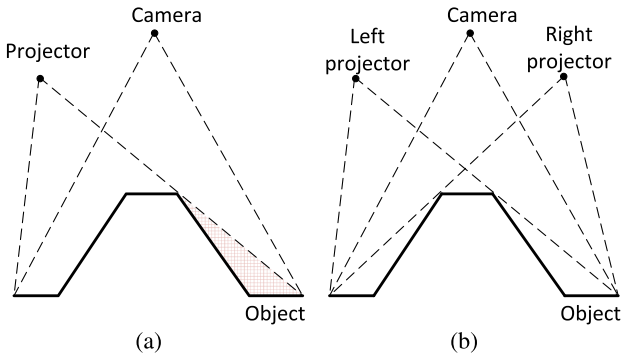

Fig. 1. Illustrations of different system setups. (a) The projector shadow problem (red grid area) from a single-projector system; (b) a dual-projector system that alleviates the shadow problem.

from two projectors are roughly aligned with each other. However, we still need to further register two patches of 3D data to achieve refined alignment. The iterative closet-point (ICP) algorithm [9–11] is widely used for 3D geometry registration. It iteratively estimates a transformation matrix for alignment by minimizing the distance between two surfaces. Although it works well, the ICP algorithm requires multiple iterations of calculation, and spiky noise in measured data may affect the optimization. We find that the residual small difference between two projector reconstruction is a function of 3D measurement value (x, y, z), which can be estimated from calibration data. In our study, a third-order residual error function is used to systematically correct misalignment. After 3D registration, we propose an angle calculation algorithm to decide higher quality data from two projectors' measurement results. Then a data fusion algorithm with linear weighting factors is designed to merge two patches of surface geometry into one single 3D shape.

Section 2 explains the principle of the proposed method, including the phase-shifting algorithm, system calibration framework, residual error correction, and 3D data fusion based on angle calculation. Section 3 shows experimental results to verify the performance of the proposed method, and Section 4 summarizes the work presented in this paper.

2. PRINCIPLE

We propose a structured light system with dual projectors to address problems caused by a single projector. A computational framework is introduced for an accurate system calibration. Then we estimate a residual error function from calibration data for 3D registration. The angle between the projection direction and surface normal is calculated to decide higher-quality data from two projectors point by point, and a data fusion algorithm is applied to generate one final measurement result.

A. Least-Squares Phase-Shifting Algorithm

For an N-step phase-shifting algorithm [12] with equal phase shifts, the kth fringe image can be mathematically represented as

$$I_k(x,y) = I'(x,y) + I''(x,y)\cos(\phi + 2k\pi/N), \quad (1)$$

where $I'(x,y)$ is the average intensity, $I''(x,y)$ is the intensity modulation, and $\phi(x,y)$ is the phase to be solved for. The ratio of $I''(x,y)$ and $I'(x,y)$ reflects the fringe contrast to environmental light, which is defined as a γ value,

$$\gamma(x,y) = I''(x,y)/I'(x,y). \quad (2)$$

One can use a threshold γ_t to remove the shadow region where the fringe contrast is too low, so that $\gamma(x,y) < \gamma_t$.

Simultaneously solving these N equations in a least-squares manner leads to

$$\phi(x,y) = -\tan^{-1}\left[\frac{\sum_{k=1}^{N} I_k \sin(2k\pi/N)}{\sum_{k=1}^{N} I_k \cos(2k\pi/N)}\right]. \quad (3)$$

Here, $\phi(x,y)$ is calculated from an arctangent function that is naturally wrapped within $(-\pi, \pi]$ with 2π discontinuities. Therefore, an additional phase-unwrapping step is needed to obtain a continuous phase map. Essentially, it adds or subtracts integer times of 2π to the wrapped phase,

$$\Phi(x,y) = \phi(x,y) + 2\pi \times k(x,y). \quad (4)$$

In this paper, we use a set of eighteen-step ($N = 18$) binary phase-shifted patterns with a fringe period of $T = 18$ pixels. Ekstrand and Zhang [13] proved that using nearly focused binary patterns in a phase-shifting method with a large step number can achieve high measurement quality, and thus nearly focused binary patterns are used for this research.

B. System Calibration

Essentially, calibration is to estimate all parameters that describe the relationship from the world coordinate system (x^w, y^w, z^w) to the image coordinate system (u, v). For both projector and camera, we use a well-known pinhole model [14] since non-telecentric lenses are used, which mathematically can be described as

$$s[u, v, 1]^T = \mathbf{A}[\mathbf{R}, \mathbf{t}][x^w, y^w, z^w, 1]^T, \quad (5)$$

where s is the scaling factor, and $[u, v, 1]^T$ represents the homogeneous image coordinate. $[\mathbf{R}, \mathbf{t}]$ denotes the extrinsic parameters with a 3×3 rotation matrix $\mathbf{R}$ and a 3×1 translation vector $\mathbf{t}$. Extrinsic parameters represent transformation relationship from the world coordinate system to the lens coordinate system. The intrinsic parameter $\mathbf{A}$ is a 3×3 matrix that describes the projection from the 3D lens coordinate to the 2D image plane.

Calibration of each individual module (i.e., camera and projector) has been well established. For intrinsic camera calibration, we use a flat calibration board with white circles printed on a black background, and the physical distances between circle centers are known. The calibration board is placed with different poses, and each pose is captured by the camera. Using the standard OpenCV camera calibration toolbox, we can extract circle centers as feature points and estimate the intrinsic camera parameters.

Although sharing the same pinhole model, the projector projects images instead of capturing images. We adopt the mapping method proposed by Zhang and Huang [15] to correspond camera and projector pixels so that the camera calibration method can be used for projector calibration. By projecting both horizontal and vertical phase-shifted patterns on the calibration board, we can retrieve absolute phase Φ_v and Φ_h using

the phase-shifting algorithm and the temporal phase unwrapping. In this study, we utilize a gray-code-based temporal phase-unwrapping algorithm [16] for absolute phase retrieval. For each camera pixel (u^c, v^c), we obtain phase value $\Phi_v^c(u^c, v^c)$ and $\Phi_h^c(u^c, v^c)$, and the corresponding projector pixel has the same phase values Φ_v^p and Φ_h^p in projector space. Since projected patterns are computer generated, the mapping relationship from the absolute phase to the projector pixel is known. The phase-shifted patterns we use only change in one direction. Therefore, Φ_v corresponds to one vertical line, and Φ_h corresponds to one horizontal line in the projector space governed by

$$\Phi_v^c(u^c, v^c) = \Phi_v^p(u^p) = \Phi_v, \tag{6}$$

$$\Phi_h^c(u^c, v^c) = \Phi_h^p(u^p) = \Phi_h. \tag{7}$$

These two lines uniquely determine the corresponding projector point (u^p, v^p) mapped from the camera pixel (u^c, v^c). Once the correspondence points are determined, those calibration feature points used for camera calibration can be used for projector calibration, and thus we can estimate intrinsic projector parameters in the same way as the camera calibration.

After intrinsic calibration, extrinsic parameters are calibrated. During extrinsic calibration, the world coordinate is built and the transformation relationship between the lens coordinate system of each device and the world coordinate system is estimated. If we calibrate each projector–camera pair separately, the world coordinates defined in each subsystem are independent of each other, and we need an additional procedure to align these two world coordinates. Therefore, we want to establish one unique world coordinate so that reconstruction results from two projectors are naturally aligned under the same 3D coordinate system. From Zhang and Yau's study [3], the world coordinate is built on the calibration board with the x and y axes parallel to the board and the z axis perpendicular to the board. If the same pose is used for all devices, the same physical point (i.e., the circle center) is chosen as the origin, and we can build a unique world coordinate system. Therefore, for extrinsic calibration, we use same poses of the calibration board for all three devices. For each pose, both projectors project patterns sequentially, and the camera captures all fringe images to extract circle centers on each image plane. Then a standard stereo camera calibration method is used for extrinsic parameter estimation. Note that for intrinsic calibration, we use different poses to calibrate each device independently.

Without losing generosity, we align the world coordinate system with the camera lens coordinate system, and now the extrinsic matrix of the camera becomes $[\mathbf{E_3}, \mathbf{0}]$, where $\mathbf{E_3}$ is a 3×3 identity matrix, and $\mathbf{0}$ is a 3×1 vector with element 0. Then the dual-projector one-camera system can be mathematically expressed as

$$s^c[u^c, v^c, 1]^T = \mathbf{A^c}[\mathbf{E_3}, \mathbf{0}][x^w, y^w, z^w, 1]^T = \mathbf{M^c}[x^w, y^w, z^w, 1]^T, \tag{8}$$

$$\begin{aligned} s_l^p[u_l^p, v_l^p, 1]^T &= \mathbf{A_l^p}[\mathbf{R_l^p}, \mathbf{t_l^p}][x^w, y^w, z^w, 1]^T \\ &= \mathbf{M_l^p}[x^w, y^w, z^w, 1]^T, \end{aligned} \tag{9}$$

$$\begin{aligned} s_r^p[u_r^p, v_r^p, 1]^T &= \mathbf{A_r^p}[\mathbf{R_r^p}, \mathbf{t_r^p}][x^w, y^w, z^w, 1]^T \\ &= \mathbf{M_r^p}[x^w, y^w, z^w, 1]^T. \end{aligned} \tag{10}$$

Here, superscripts ^{c}, ^{p_l}, and ^{p_r} represent the parameters of the camera, left projector, and right projector, respectively. $\mathbf{M^c}$, $\mathbf{M_l^p}$, and $\mathbf{M_r^p}$ are a combination of extrinsic and intrinsic parameters for the sake of simplicity. Once the system is calibrated, $\mathbf{M^c}$, $\mathbf{M_l^p}$, and $\mathbf{M_r^p}$ are determined. Then, from the left projector and camera, we can determine unknowns $(s^c, s_l^p, x^w, y^w, z^w)$ by simultaneously solving Eqs. (6)–(9) by a least-squares algorithm. Similarly, from the right projector and camera, we can also reconstruct a 3D result (x^w, y^w, z^w) by solving Eqs. (6)–(8) and Eq. (10) together.

C. 3D Data Fusion

Ideally, after system calibration under the same world coordinate, 3D results recovered from two projector–camera pairs are supposed to align accurately. However, the alignment is not perfect in practice due to the existence of lens imperfection, errors in modeling, and/or parameter estimation. For example, from our experiment data, the 3D circle centers reconstructed from two projectors have roughly ± 0.1 mm difference in the x and y axis, and the z coordinate difference is within $(-1.1, 0.9)$mm.

Chen *et al.* [17] proposed a method to improve the circle-pattern-based calibration by refining the circle edge detection and iteratively compensating for the calibration error caused by inaccurate circle center locations. In this study, we propose to fit a residual error function from calibration data to compensate for the residual small misalignments. Using the calibrated parameters, we can reconstruct the 3D coordinates of calibration board circle centers. Suppose $\mathbf{X_l} = (x_l, y_l, z_l)$ and $\mathbf{X_r} = (x_r, y_r, z_r)$ are reconstructed 3D coordinates from the left and right projector, respectively. Then we can take the difference of measurement results for the same circle center,

$$\Delta\mathbf{X} = \mathbf{X_r} - \mathbf{X_l}, \tag{11}$$

where vector $\Delta\mathbf{X} = (\Delta x, \Delta y, \Delta z)$ is the alignment error along the x, y, z directions. We assume that each projector contributes to half of the residual error, and a third-order error function is used to estimate $\Delta\mathbf{X}$, which mathematically can be modeled as

$$\frac{1}{2}\Delta\mathbf{X^T} = \mathbf{c_l} + \mathbf{d_l}\tilde{\mathbf{X}}_\mathbf{l}, \tag{12}$$

where $\tilde{\mathbf{X}}_\mathbf{l} = \{x_l, y_l, z_l, x_l^2, y_l^2, z_l^2, x_l y_l, x_l z_l, y_l z_l, x_l^3, y_l^3, z_l^3, x_l^2 y_l, x_l^2 z_l, x_l y_l^2, x_l z_l^2, y_l^2 z_l, y_l z_l^2, x_l y_l z_l\}^T$, coefficient parameter $\mathbf{c_l}$ is a 3×1 vector, and $\mathbf{d_l}$ is a 3×19 matrix. To estimate all parameters in Eq. (12), we need at least 20 circle centers. In our algorithm, we apply all circle center data used in system calibration to solve $\mathbf{c_l}$ and $\mathbf{d_l}$ by a least-squares algorithm. Once all parameters are decided, we can apply this fitted model to correct any 3D measurement from the left projector by

$$\mathbf{X_{lc}^T} = \mathbf{X_l^T} + \mathbf{c_l} + \mathbf{d_l}\tilde{\mathbf{X}}_\mathbf{l}. \tag{13}$$

Here $\mathbf{X_{lc}} = (x_{lc}, y_{lc}, z_{lc})$ is the corrected 3D coordinate for left projector results. Similarly, we can also estimate an error function for the right projector with the model

$$\frac{1}{2}\Delta\mathbf{X}^{\mathbf{T}} = \mathbf{c_r} + \mathbf{d_r}\tilde{\mathbf{X}}_\mathbf{r}, \tag{14}$$

where $\tilde{\mathbf{X}}_\mathbf{r} = \{x_r, y_r, z_r, x_r^2, y_r^2, z_r^2, x_r y_r, x_r z_r, y_r z_r, x_r^3, y_r^3, z_r^3, x_r^2 y_r, x_r^2 z_r, x_r y_r^2, x_r z_r^2, y_r^2 z_r, y_r z_r^2, x_r y_r z_r\}^T$, coefficient parameter $\mathbf{c_r}$ is a 3×1 vector, and $\mathbf{d_r}$ is a 3×19 matrix. Then we apply the estimated error function to the right projector 3D measurement by

$$\mathbf{X}_{\mathbf{rc}}^{\mathbf{T}} = \mathbf{X}_{\mathbf{r}}^{\mathbf{T}} + \mathbf{c_r} + \mathbf{d_r}\tilde{\mathbf{X}}_\mathbf{r}. \tag{15}$$

Here $\mathbf{X_{rc}} = (x_{rc}, y_{rc}, z_{rc})$ is the corrected 3D coordinate of the right projector results.

After 3D alignment refinements, we fuse two sets of data into one final result. During measurements, two projectors shine light from different angles, and projected fringe patterns are distorted by object surface geometry. Figure 2(a) illustrates the projection model from the projector to object. $(O^p; x^p, y^p, z^p)$ is projector lens coordinate, O^pQ is the projection light to the object point Q, the vector $\mathbf{m} = \overrightarrow{QO^p}$ denotes the projection direction, the surface normal of Q is represented by $\mathbf{n}$, and the projection angle between $\mathbf{m}$ and $\mathbf{n}$ is θ. O^pA and O^pB are two light rays that come from the projector with $AB \perp O^pQ$, and they propagate to the object surface as points A' and B, followed by

$$|A'B'| = \frac{|AB|}{|\cos\theta|}. \tag{16}$$

Assume the phase difference between A and B on the projector pattern is $\Delta\Phi$, and then the phase difference between A' and B' is also $\Delta\Phi$. Because the phase changes fastest on $|AB|$, we can use θ to quantify phase quality near point Q, since smaller θ means $|A'B'|$ is shorter, and thus projected fringe patterns on the object surface have a higher frequency (i.e., change quicker).

The calculation of projection direction vector $\mathbf{m}$ is straightforward. Assume the world coordinate of point Q is (x_Q, y_Q, z_Q). Under the projector lens coordinate, O^p is the origin (0, 0, 0), and the corresponding coordinate in world coordinate can be calculated from extrinsic parameters between the projector and world coordinate followed by

$$[0,0,0]^T = [\mathbf{R^p}, \mathbf{t^p}][x_{O^p}, y_{O^p}, z_{O^p}, 1]^T, \tag{17}$$

$$\mathbf{m} = (x_{O^p} - x_Q, y_{O^p} - y_Q, z_{O^p} - z_Q). \tag{18}$$

Here, $(x_{O^p}, y_{O^p}, z_{O^p})$ is a transferred world coordinate point from (0, 0, 0) in the projector coordinate, and $\mathbf{m}$ is the projection direction vector under the world coordinate. Since $[\mathbf{R^p}, \mathbf{t^p}]$ is obtained from calibration, Eq. (17) has three unknowns and three equations. Then $(x_{O^p}, y_{O^p}, z_{O^p})$ can be calculated by simultaneously solving these three linear equations.

The calculation of the surface normal based on reconstructed 3D data is illustrated in Fig. 2(b). To obtain the surface normal of point $Q(u, v)$, we first connect it with its neighbor 3D points $\{V_{u-1,v-1}, V_{u,v-1}, \ldots, V_{u+1,v+1}\}$ to form 8 triangulations. The vector from point Q to its neighborhood is denoted as $\mathbf{k_i}$. Then within each triangulation, we calculate the normalized normal vector $\mathbf{n_i}$ by

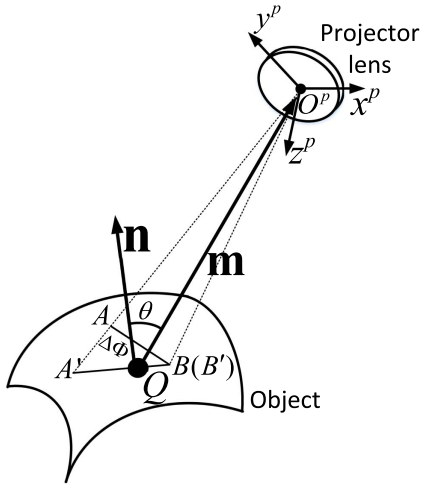

(a)

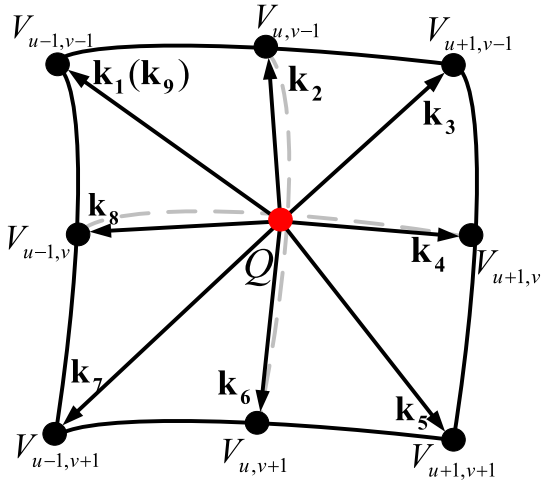

(b)

Fig. 2. Illustrations of angle calculation for data merging algorithm. (a) A demonstration of pattern projection from projector to object surface; (b) a diagram of surface normal calculation.

$$\mathbf{n}_i = \frac{\mathbf{k_i} \times \mathbf{k_{i+1}}}{|\mathbf{k_i} \times \mathbf{k_{i+1}}|}, \qquad i = 1, 2, \ldots, 8. \tag{19}$$

The final normal vector for point Q is determined by taking the average of all triangulation normals to avoid bias in any direction,

$$\mathbf{n} = \frac{1}{8}\sum_{i=1}^{8} \mathbf{n}_i. \tag{20}$$

After calculating vectors $\mathbf{m}$ and $\mathbf{n}$, the projection angle θ between the surface normal $\mathbf{n}$ and projection direction $\mathbf{m}$ can be calculated as

$$\theta = \tan^{-1}\left(\frac{|\mathbf{m} \times \mathbf{n}|}{\mathbf{m} \cdot \mathbf{n}}\right). \tag{21}$$

For both projector-camera pairs, we can calculate the angle θ_l and θ_r on each of the recovered 3D points, and data points with smaller θ have higher measurement accuracy. Here, we

define an angle difference threshold δ. If the calculated angle difference between the left and right projector is within δ, we combine 3D data from two subsystems with a weighting factor determined by angle difference. If the angle difference is larger than δ, we select the 3D point with smaller angle θ, which provides better measurement quality to the final measurement result. The mathematical equation of the proposed 3D data fusion algorithm can be expressed as

$$\mathbf{X} = \begin{cases} \mathbf{X_l} & \text{if } \theta_l(u,v) - \theta_r(u,v) > \delta; \\ \mathbf{X_r} & \text{if } \theta_l(u,v) - \theta_r(u,v) < -\delta; \\ a\mathbf{X_l} + (1-a)\mathbf{X_r} & \text{otherwise.} \end{cases} \tag{22}$$

Here, the weighting factor

$$a = (\theta_l(u,v) - \theta_r(u,v) + \delta)/2\delta. \tag{23}$$

3. EXPERIMENT

We experimentally verified the proposed method by developing a 3D shape measurement system with two projectors and one camera. Figure 3 shows a photograph of the actual measurement system. The system is configured symmetrically: the camera is put in the middle, and two projectors on two sides have similar distance and angle to the camera.

In this system, the projectors we used are digital-light-processing (DLP) projectors (model: Optoma ML750) with a resolution of 1280×800. The projector lens has a 14.95 mm focal length with an aperture of $f/2.0$, and focus distance ranges between 97 and 258 cm. The camera is a complementary metal-oxide-semiconductor (CMOS) camera (model: Point Grey Grasshopper 3) whose resolution is chosen as 640×480. The camera is attached with a pinhole lens (model: Computar M0814-MP2) with an 8 mm focal length and an aperture of $f/1.4$.

During the calibration stage, we placed the calibration board in 25 different poses for each device and estimated corresponding intrinsic parameters independently. The calibrated intrinsic parameters for the experiment setup are

$$\mathbf{A^c} = \begin{bmatrix} 1418.997 & 0 & 319.427 \\ 0 & 1419.427 & 243.861 \\ 0 & 0 & 1 \end{bmatrix}, \tag{24}$$

$$\mathbf{A^{P_l}} = \begin{bmatrix} 1946.797 & 0 & 609.534 \\ 0 & 1946.335 & 1.013 \\ 0 & 0 & 1 \end{bmatrix}, \tag{25}$$

$$\mathbf{A^{P_r}} = \begin{bmatrix} 1957.640 & 0 & 654.574 \\ 0 & 1957.916 & 708.125 \\ 0 & 0 & 1 \end{bmatrix}. \tag{26}$$

Here $\mathbf{A^c}$, $\mathbf{A^{P_l}}$, and $\mathbf{A^{P_r}}$ are intrinsic matrices of the camera, left projector, and right projector, respectively, all in pixels. Then we used another 10 poses for extrinsic calibration. For each pose, the left projector and the right projector separately projected fringe patterns on the calibration board, and the camera captured all images. The estimated extrinsic matrices for the camera, left projector, and right projector are denoted as $[\mathbf{R^c}, \mathbf{t^c}]$, $[\mathbf{R_l^P}, \mathbf{t_l^P}]$, and $[\mathbf{R_r^P}, \mathbf{t_r^P}]$, which in our experiment are

$$\mathbf{R^c} = \begin{bmatrix} 1 & 0 & 0 \\ 0 & 1 & 0 \\ 0 & 0 & 1 \end{bmatrix}, \quad \mathbf{t^c} = \begin{bmatrix} 0 \\ 0 \\ 0 \end{bmatrix}, \tag{27}$$

$$\mathbf{R_l^P} = \begin{bmatrix} 0.999260 & 0.024337 & -0.029797 \\ -0.026617 & 0.996545 & -0.078676 \\ 0.027779 & 0.079411 & 0.996455 \end{bmatrix},$$

$$\mathbf{t_l^P} = \begin{bmatrix} 21.973540 \\ 141.137006 \\ -10.072587 \end{bmatrix}, \tag{28}$$

$$\mathbf{R_r^P} = \begin{bmatrix} 0.999745 & 0.019855 & -0.010773 \\ -0.018495 & 0.993271 & 0.114323 \\ 0.012970 & -0.114095 & 0.993385 \end{bmatrix},$$

$$\mathbf{t_r^P} = \begin{bmatrix} 6.295695 \\ -151.703955 \\ -11.708740 \end{bmatrix}. \tag{29}$$

To evaluate the performance of our proposed method, we first measured a smooth sphere with a radius of 97.95 mm. Figure 4 shows experimental results from each camera–projector pair. Fringe images from the left and right projector

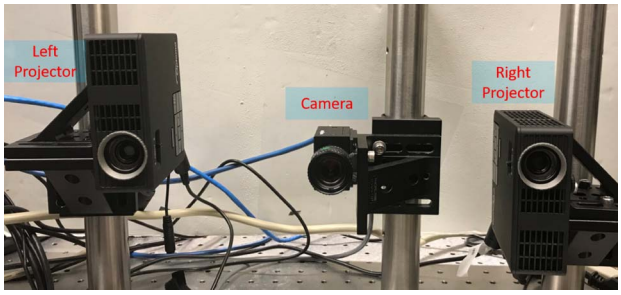

Fig. 3. Photograph of the proposed dual-projector single-camera 3D measurement system.

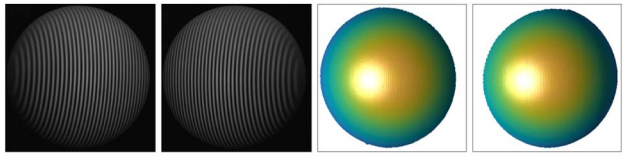

Fig. 4. Sphere 3D measurement by single-projector system. (a) One of fringe patterns from the left projector fringe images; (b) one of fringe patterns from the right projector fringe images; (c) 3D reconstruction using the fringe patterns projected by the left projector; (d) 3D reconstruction using the fringe patterns projected by the right projector.

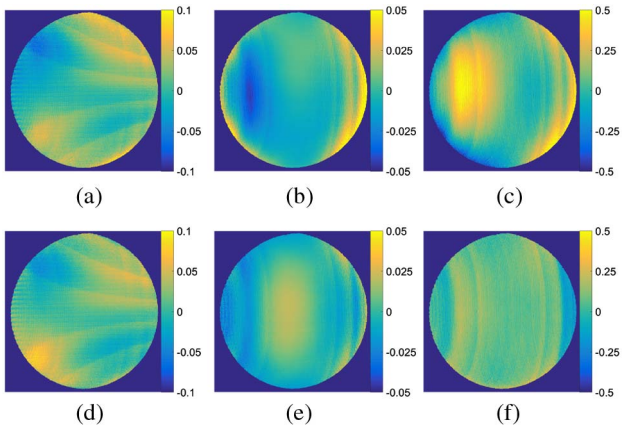

Fig. 5. Difference maps of 3D results from Figs. 4(c) and 4(d). (a) x coordinate difference map before correction (mean error: 0.011 mm; standard deviation: 0.027 mm); (b) y coordinate difference map before correction (mean error: −0.002 mm; standard deviation: 0.017 mm); (c) z coordinate difference map before correction (mean error: 0.111 mm; standard deviation: 0.175 mm); (d) x coordinate difference map after correction (mean error: 0.015 mm; standard deviation: 0.023 mm); (e) y coordinate difference map after correction (mean error: −0.001 mm; standard deviation: 0.012 mm); (f) z coordinate difference map after correction (mean error: 0.067 mm; standard deviation: 0.080 mm).

are shown in Figs. 4(a) and 4(b), and the corresponding 3D results are shown in Figs. 4(c) and 4(d).

To compare 3D results from two camera–projector pairs, we calculated difference maps for the x, y, z coordinates, which are presented in Figs. 5(a)–5(c). Compared with the x and y coordinate difference (roughly ± 0.1 mm for x and ± 0.05 mm for y), the z coordinate has a relatively larger difference of ± 0.5 mm. By implementing the proposed residual error correction algorithm, we calculated difference maps for corrected 3D results as illustrated in Figs. 5(d)–5(f). After the error correction, the coordinate difference between two 3D patches becomes smaller with more uniform distribution, which demonstrates better alignment in geometry.

Then we merged the two projectors' data into one single 3D, and the results are shown in Fig. 6. On each 3D point, we calculated the projection angle θ between the surface normal and the projection direction. Based on the angle calculation,

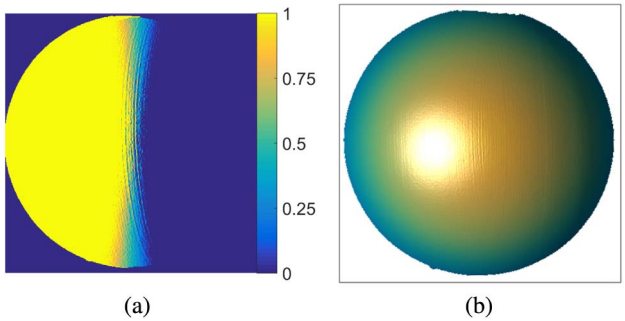

Fig. 6. Measurement results by proposed dual-projector system. (a) The weighting factor map; (b) final 3D geometry of the sphere.

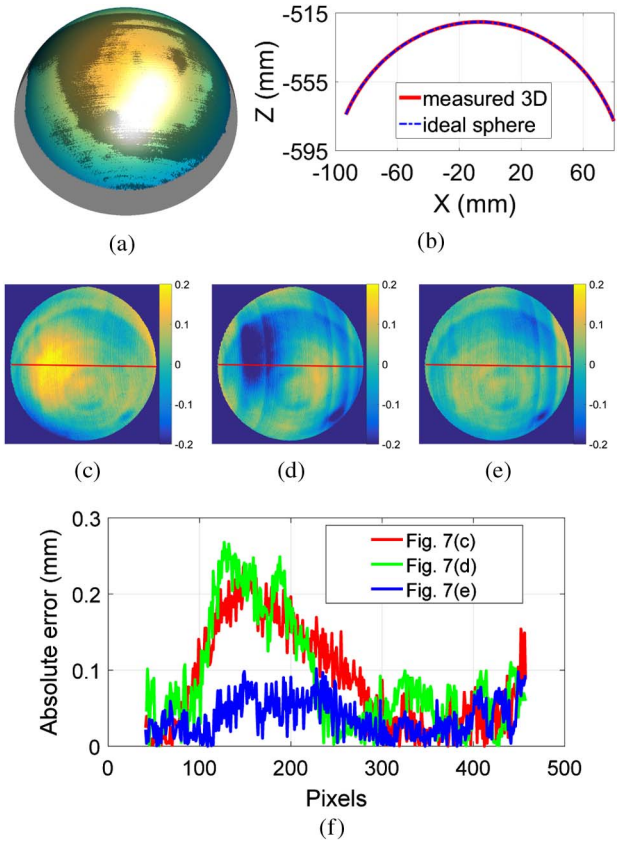

Fig. 7. Error analysis on sphere measurement. (a) The overlap of measured 3D and fitted ideal sphere; (b) one cross section of depth curve from (a); (c) error map of the 3D results shown in Fig. 4(c) (mean error: 0.041 mm; standard deviation: 0.069 mm); (d) error map of the 3D results shown in Fig. 4(d) (mean error: −0.048 mm; standard deviation: 0.086 mm); (e) error map of final 3D result shown in Fig. 6(b) (mean error: −0.004 mm; standard deviation: 0.053 mm); (f) one cross section of error maps in (c)–(e).

we generated the weighting factor map as shown in Fig. 6(a) by using Eq. (23). In our experiment, we set the angle difference threshold $\delta = 5°$. In the middle region of the sphere, the angle difference between two projectors is small, and thus the weighting factor a gradually changes within (0, 1) to linearly

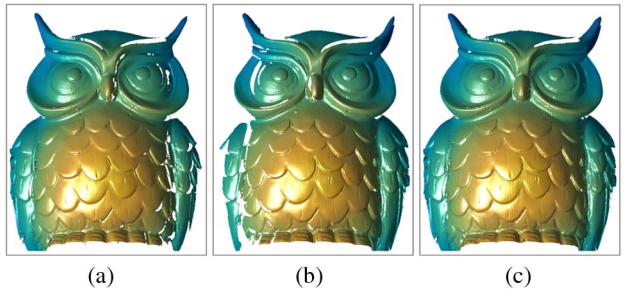

Fig. 8. 3D measurement results of a complex statue. (a) 3D reconstruction using fringe patterns projected from the left projector; (b) 3D reconstruction using fringe patterns projected from the right projector; (c) 3D result by combining (a) and (b) using our proposed method.

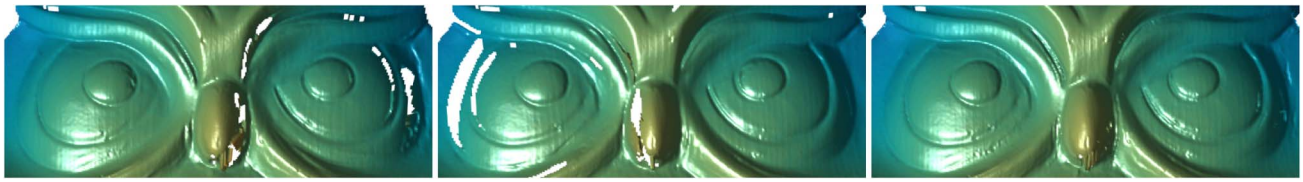

(a) (b) (c)

Fig. 9. Close-up views of the 3D results shown in Fig. 8. (a) Zoom-in view of Fig. 8(a); (b) zoom-in view of Fig. 8(b); (c) zoom-in view of Fig. 8(c).

combine data from two projectors. When the angle difference is larger than δ, we simply selected the 3D data with smaller θ. Figure 6(b) presents the final 3D result after applying the data fusion algorithm.

We analyzed the accuracy of the merged data, comparing with the raw measured data. Figure 7 shows the result. We used the raw 3D data from both projectors to fit an ideal sphere. Figure 7(a) shows the geometry of the final 3D measurement that is overlapped with the ideal sphere model, and Fig. 7(b) shows one cross section of depth (z) curve. To further compare the measurement error, we subtracted the measured data from the ideal sphere and generated error maps for 3D results from the left projector, right projector, and final combined measurement, which are shown in Figs. 7(c)–7(e). After the residual error correction and data fusion, we achieved better measurement accuracy for the sphere: the mean error is reduced to −0.004 mm, and the standard deviation is reduced to 0.053 mm. We also took the same cross section of the error maps and compared them in Fig. 7(f). This figure clearly demonstrated that the measurement error is smaller for the fused data compared with any individual sub-projector–camera system.

It is worth noting that there exist some structural errors in Figs. 7(c)–7(e). We have confirmed that such structural errors were caused by the imperfection of the digital micro-mirror device (DMD) used in the projector, but not by the calibration error, since such structural error aligned with the projector lines. Furthermore, we noticed that this type of error is independent of the measurement, and thus our system's residual error compensation method does not reduce this structural error.

To further verify the performance of the proposed dual-projector-based measurement framework, we captured an owl statue with more complex surface geometry. Figure 8 presents a measurement results comparison from the single-projector system and dual-projector system. Because each projector illuminates the object in a specific angle and the statue has a complicated geometry, shadow problems are created on the nose, eyes, and wing areas. These shadow regions are removed by a threshold $\gamma_t = 0.15$, and the corresponding 3D reconstruction has missing data as shown in Figs. 8(a) and 8(b).

After applying the residual error correction, we calculated weighting factor map and applied a data fusion algorithm to generate the final measurement result, which is shown in Fig. 8(c). The final result merged from two 3D patches has a complete measurement on both the head and wing areas. Figure 9 shows a comparison of a zoomed-in view of the same head region. It can be observed that the nose and eyes geometry cannot be properly reconstructed by either single projector, while after data fusion we obtained satisfying results. The experiment results reveal that the proposed dual-projector measurement framework can alleviate the shadow problem caused by the single projection device.

4. SUMMARY

We have presented a structured light system with dual projectors and a single camera to enhance the measurement capabilities of the single-projector single-camera system. To achieve high-quality 3D shape measurement, a calibration framework was developed, a residual error correction algorithm was proposed, and a data fusion algorithm based on projection angle calculation was proposed to merge two patches of geometry into a single profile. Experimental results demonstrated that the proposed system can simultaneously reduce shadow problems caused by single projector illumination and enhance measurement accuracy by 3D data fusion.

Funding. Directorate for Engineering (ENG) (CMMI-1531048).

REFERENCES

1. S. Zhang, "Recent progresses on real-time 3D shape measurement using digital fringe projection techniques," Opt. Laser Eng. **48**, 149–158 (2010).
2. S. S. Gorthi and P. Rastogi, "Fringe projection techniques: whither we are?" Opt. Laser Eng. **48**, 133–140 (2010).
3. S. Zhang and S.-T. Yau, "Three-dimensional shape measurement using a structured light system with dual cameras," Opt. Eng. **47**, 013604 (2008).
4. W. Zhang, H. Zhao, and X. Zhou, "Multiresolution three-dimensional measurement system with multiple cameras and light sectioning method," Opt. Eng. **49**, 123601 (2010).
5. G.-H. Liu, X.-Y. Liu, and Q.-Y. Feng, "3D shape measurement of objects with high dynamic range of surface reflectivity," Appl. Opt. **50**, 4557–4565 (2011).
6. C. Jiang and S. Zhang, "Absolute phase unwrapping for dual-camera system without embedding statistical features," Opt. Eng. **56**, 094114 (2017).
7. W. Lohry, V. Chen, and S. Zhang, "Absolute three-dimensional shape measurement using coded fringe patterns without phase unwrapping or projector calibration," Opt. Express **22**, 1287–1301 (2014).
8. Z. Li, K. Zhong, Y. F. Li, X. Zhou, and Y. Shi, "Multiview phase shifting: a full-resolution and high-speed 3D measurement framework for arbitrary shape dynamic objects," Opt. Lett. **38**, 1389–1391 (2013).
9. P. J. Besl and N. D. McKay, "A method for registration of 3-D shapes," IEEE Trans. Pattern Anal. Mach. Intell. **14**, 239–256 (1992).
10. Z. Zhang, "Iterative point matching for registration of free-form curves and surfaces," Int. J. Comput. Vis. **13**, 119–152 (1994).

11. S. Rusinkiewicz and M. Levoy, "Efficient variants of the ICP algorithm," in *3rd International Conference on 3-D Digital Imaging and Modeling* (IEEE, 2001), pp. 145–152.
12. J. E. Greivenkamp, "Generalized data reduction for heterodyne interferometry," Opt. Eng. **23**, 234350 (1984).
13. L. Ekstrand and S. Zhang, "Three-dimensional profilometry with nearly focused binary phase-shifting algorithms," Opt. Lett. **36**, 4518–4520 (2011).
14. Z. Zhang, "A flexible new technique for camera calibration," IEEE Trans. Pattern Anal. Mach. Intell. **22**, 1330–1334 (2000).
15. S. Zhang and P. S. Huang, "Novel method for structured light system calibration," Opt. Eng. **45**, 083601 (2006).
16. G. Sansoni, M. Carocci, and R. Rodella, "Three-dimensional vision based on a combination of gray-code and phase-shift light projection: Analysis and compensation of the systematic errors," Appl. Opt. **38**, 6565–6573 (1999).
17. R. Chen, J. Xu, H. Chen, J. Su, Z. Zhang, and K. Chen, "Accurate calibration method for camera and projector in fringe patterns measurement system," Appl. Opt. **55**, 4293–4300 (2016).